https://doi.org/10.26599/JAC.2024.9220908

Research Article

The role of γ-$C_2H_5NO_2$ as a new transient liquid phase in cold sintering process of $BaTiO_3$ composites

Jitrawan Noisak [a,b], Pimchanok Ieamviteevanich [a], Thitirat Charoonsuk [c], Phakkhananan Pakawanit [d], Nattapong Pinpru [e], Wanwilai Vittayakorn [f], Tosapol Maluangnont [f], Panpailin Seeharaj [a], Theerachai Bongkarn [g,h], Te-Wei Chiu [i], Naratip Vittayakorn [a,b *]

[a] *Advanced Materials Research Unit, School of Science, King Mongkut's Institute of Technology Ladkrabang, Bangkok 10520, Thailand*
[b] *Department of Chemistry, School of Science, King Mongkut's Institute of Technology Ladkrabang, Bangkok 10520, Thailand*
[c] *Department of Materials Science, Faculty of Science, Srinakharinwirot University, Sukhumvit 23, Wattana, Bangkok 10110, Thailand*
[d] *Synchrotron Research and Applications Division, Synchrotron Light Research Institute, 111 University Avenue, Muang District, Nakhon Ratchasima 30000, Thailand*
[e] *Sustainability Centre, Plastics Market Intelligent Department, Plastics Institute of Thailand, Bangkok 10110, Thailand*
[f] *Electroceramics Research Laboratory, College of Materials Innovation and Technology, King Mongkut's Institute of Technology Ladkrabang, Bangkok 10520, Thailand*
[g] *Department of Physics, Faculty of Science, Naresuan University, Phitsanulok 65000, Thailand*
[h] *Research Center for Academic Excellence in Applied Physics, Faculty of Science, Naresuan University, Phitsanulok 65000, Thailand*
[i] *Department of Materials and Mineral Resources Engineering, "National" Taipei University of Technology, Taipei 106, Taiwan, China*

*Corresponding author.
E-mail: naratip.vi@kmitl.ac.th

Received: March 03, 2024; Revised: April 12, 2024; Accepted: May 01, 2024

Abstract: Dielectric materials, like barium titanate-based (BT-based), have excellent dielectric properties but require high temperatures (above 1300 ˚C) for ceramic fabrication, leading to high costs and energy loss. The cold sintering process (CSP) offers a solution to these issues and is gaining worldwide attention as an innovative fabrication route. In this work, we proposed an alternative organic ferroelectric phase, gamma-glycine (γ-GC) that acts as a transient liquid phase to fabricate high-density composites with barium titanate (BT) at low-temperature through a CSP. Our findings show that the density of 15γ-GC/85BT reached 96.7±1.6% when sintered at 120 ˚C for 6 hours (h) under 10MPa uniaxial pressure. The SEM-EDS mapping of the composite suggested that γ-GC completely underwent the precipitation-dissolution process and, therefore, filled between BT particles. Moreover, XRD and FTIR confirmed the preservation of γ-GC without the undesired phase transformation. In addition, the ferroelectric and dielectric properties of the γ-GC/BT composites were reported. The high dielectric constant (ε_r) was 3600, and the low dielectric loss (tan δ) was 1.20 at 200 ˚C, 100 kHz, with 15γ-GC/85BT composite. The hysteresis loop showed a remanent polarization (P_r) of 0.55 μC.cm^{-2} and a coercive field (E_c) of 7.25 kV.cm^{-1}. Our findings reaffirmed that organic ferroelectric material (γ-GC) can act as a transient liquid phase in a CSP that can successfully and sustainably fabricate γ-GC/BT composites at low temperatures while delivering outstandingly high performance.

Keywords: γ-GC, barium titanate; cold sintering process; Organic Ferroelectric Materials; Dielectric properties; Ferroelectric properties

1 Introduction

In recent years, a groundbreaking low-temperature sintering technique known as the cold sintering process (CSP) was discovered by Randall *et al.* [1] at Pennsylvania State University in 2016, has emerged as a highly effective method for producing dense ceramic materials. The CSP involves homogenizing powdered inorganic compounds with a transient liquid phase. This blending process yields a uniform mixture characterized by the presence of a transient liquid phase, typically constituting 1 to 10% of the total volume. Utilizing pressures ranging from 100 MPa to 700 MPa and temperatures below 300°C, CSP facilitates the evaporation of solvents and the densification of inorganic compounds, resulting in the formation of high-density sintered materials [2] . The core processing variables of CSP, including the transient liquid phase, sintering temperature, pressure, and holding time, play pivotal roles in driving the densification process of materials [3]. Of particular significance, the transient liquid phase substantially contributes to the dissolution-precipitation phenomenon within CSP. This mechanism enables the partial dissolution of sharp particle edges, thereby creating spaces for particle rearrangement. Moreover, the liquid phase readily redistributes itself, filling particle interstitials and fostering grain growth [4]. CSP has been successfully applied to water-soluble materials such as sodium chloride (NaCl), where NaCl particles diffuse throughout the water film, filling voids and precipitating through the dissolution-precipitation process inherent to CSP. Consequently, CSP can achieve high relative densities exceeding 90% after 24 h at room temperature and 75% relative humidity. Furthermore, CSP has been effectively employed with various metal oxide and dielectric materials, including KH_2PO_4, $NaNO_2$, and $BaTiO_3$; BT [5, 6]. Notably, KH_2PO_4 and $NaNO_2$ exhibit high relative densities (>98%) comparable to conventionally sintered materials, even when treated at temperatures below 120 ˚C under 350 MPa without additional treatment.

However, for materials with low water solubility, a tailored liquid solution becomes imperative. In a similar vein, Hanzheng Guo *et al*. [7] employed CSP to fabricate high-density BT ceramic at temperatures below 200 ˚C. By utilizing a 25wt% $Ba(OH)_2/TiO_2$ solution as a transient liquid phase and consolidating at 180°C under 430 MPa pressure, they achieved a relative density of 95%. However, a subsequent annealing step at 900 ˚C, while achieving characteristics comparable to conventionally sintered counterparts, nullified the advantage of low-temperature manufacturing, preventing the production of new composites below 300 ˚C. Addressing the limitation, Tsuji *et al.* [8] successfully fabricated dense and high-quality BT materials via cold sintering at 300 ˚C in single-step using NaOH-KOH eutectic fluxes. Nevertheless, the severe conditions of strong alkaline fluxes at 300 ˚C restrict the fabrication of innovative composites with additives such as polymers, 2D materials, and fibers due to the necessity of appropriate quick kinetics for the congruent dissolution of the ceramic phase's surface ions to ensure dense ceramic manufacturing.

Despite these challenges, recent studies have demonstrated the feasibility of co-sintering various materials through CSP, enabling the fabrication of novel composite materials. Notably, low melting point materials such as thermoplastic [9], thermosetting [10], and 2D-nanostructured materials [11] can serve as transient liquid phases in CSP, modifying matrix material qualities including density, strength, hardness, and electrical properties [12, 13]. For instance, Jing Guo et al. [11] conducted CSP to manufacture a cold co-sintering process of 2D-MXene and ZnO at 300 ˚C for 1 hour under 250 MPa pressure, resulting in improved electrical conductivity with the addition of up to 5wt% $Ti_3C_2T_x$ MXene. Takao Sada *et al.* [14] successfully co-sintered BT and PTFE using $Ba(OH)_2 \cdot 8H_2O$ flux, bridging the temperature gap between ferroelectric ceramics and polymers, albeit with challenges related to non-homogeneous polymer distribution. Similarly,

Subramaniyan Vinoth and Sea-Fue Wang [15] effectively prepared BT/poly(vinylidene difluoride) nanocomposites, albeit with issues regarding the homogeneity of polymer distribution and unclear ferroelectric properties attributed to grain boundary microstructure [16]. In our previous work, we found that organic ferroelectric materials, including γ-GC, can be fabricated into a composite with bacterial cellulose (BC) powder via CSP and achieved satisfactory ferroelectric effects at conditions 120 ˚ C/24h [17]. The γ-GC is the thermodynamically most stable phase and exhibits piezoelectric effects at room temperature because it has a winding hydrogen bond network, unlike the other two main phases (α and β phase) [18, 19]. Moreover, its water solubility qualifies it for usage as a transient liquid phase in a CSP [20, 21].

The present study proposes the use of γ-GC phase to fabricate ferroelectric composites via the cold sintering process (CSP). The γ-GC phase is an ideal transient liquid phase that induces excellent dissolution-precipitation phenomena during the CSP. Moreover, it exhibits remarkable ferroelectric properties that do not interfere with the properties of the primary phase. The focus of this research is to determine the optimized quantity of γ-GC phase for high-density BT composite through the CSP. A comprehensive examination of the time and temperature conditions applied in the CSP is conducted to refine the fabrication process and enhance the overall performance of the resulting composites.

2 Experimental

2.1 Gamma glycine (γ-GC) preparation

The γ-GC compound was synthesized using a method described in literature [17]. Firstly, 56 g of commercial-grade glycine and 15 g of sodium chloride in a 3:1 molar ratio were dissolved in 100 mL of deionized water (DI water) by stirring for 5 h at room temperature (RT). The resulting mixture was then filtered using vacuum filtration, and the obtained liquid was kept in an oven at

35 ˚C for 25 days. During this aging process, α-GC crystals were transformed into γ-GC crystals. The γ-GC crystals were then washed with saturated glycine solution, ground for 3 h using a ball mill, and finally placed in the oven for an additional 2 days. This process resulted in the successful synthesis of γ-GC crystals.

2.2 Barium titanate (BT) preparation

Two types of BT powders were employed: (i) as purchased, a commercial product from Inframat Advanced Materials, LLC ($BaTiO_3$ nano-powder, 99.95%), and (ii) Heat-treated commercial BT powder at 1200 ˚C for 12 h in air. Both powders (untreated, and heat-treated) were separately stirred with 1 M acetic acid solution at 80 ˚C for 1 h. Then, the pH of the suspension was adjusted to neutral, and the respective BT powders were filtered prior to drying in an oven at 60 ˚C for 24 h, as schematically shown in Fig. 1a.

2.3 Fabrication of γ-GC/BT composites via CSP

To optimize packing density, a specific ratio of 73.6/26.4, determined by theoretical predictions for dense random packing, was employed for mixing BT particles of both nanometer (untreated particles) and micrometer (heat-treated particles) sizes. Subsequently, the fabrication process of composites involving γ-GC and BT via CSP was initiated by precisely measuring 2.208 g of heat-treated BT and 0.792 g of untreated BT. These two types of BT were thoroughly combined in a mortar for a duration of 5 minutes to ensure homogeneity. Following this, varying proportions (15%, 30%, 50%, and 90% by weight) of γ-GC powder were incorporated into the BT mixture and meticulously blended manually in the mortar for an additional 5 minutes. Subsequently, 7wt% of DI water was introduced into the blend, which was then ground for an additional 5 minutes to facilitate thorough mixing. Next, 0.3 grams of the resulting γ-GC/BT

mixture were meticulously deposited into a tungsten carbide die. In the context of the CSP, the initial mixture undergoes continuous compression via a straightforward uniaxial pressure of 10 MPa. Heating is facilitated by a resistance jacket enveloping the die system within the CS equipment employed. The heating jacket demonstrates the capability to ramp up the temperature at a steady rate of 3°C per minute, reaching a maximum temperature of 120°C. The specified heating temperature and duration were maintained for 6 hours. The CSP apparatus utilized in this investigation was constructed as depicted in Figure 1b (I-III). Once the process was completed, the cold-sintered γ-GC/BT composite was allowed to cool before being extracted from the block for subsequent characterization analysis.

2.4 Characterization

Although the Archimedes method is renowned for its precision in determining density, its utility in our investigation was hampered by the solubility properties of γ-GC in polar solvents. Traditional organic solvents employed in Archimedes' principle, such as water, ethanol, isopropanol, and acetone, were deemed incompatible with our samples due to their inherent polarity. Moreover, the use of nonpolar solvents posed a risk of altering the phase or stability of γ-GC. Additionally, the metastable nature of γ-GC warranted cautious immersion protocols, as it could lead to phase transitions in glycine. Consequently, we adopted an alternative approach to determine sample density, relying on measurements of mass, thickness, and dimensions. By employing 12 samples, we aimed to account for inherent variations within the sample set, thereby obtaining a more comprehensive representation of density. Densification calculations were performed using Equation (1), elucidating the ratio of actual density to theoretical density [17, 22].

$$R = \frac{4m}{(\pi d^2 h \rho)} \times 100\% \quad (1)$$

where R is the relative density (%), m is the mass (g) of the pellet, d is the diameter (cm) of the pellet, h is the thickness (cm) of the pellet, and ρ is the theoretical density calculated from the Eq. (2)

$$\rho = \frac{m}{(\frac{m_{BT}}{\rho_{BT}} + \frac{m_{\gamma-GC}}{\rho_{\gamma-GC}})} \quad (2)$$

where m_{BT} and $m_{\gamma-GC}$ represent the masses of BT and γ-GC in the composite pellet; ρ_{BT} and $\rho_{\gamma-GC}$ represent the theoretical densities of BT and γ-GC, which are 6.02 g·cm^{-3} and 1.59 g·cm^{-3}, respectively [17, 23].

The phase purity and crystal structure of the cold-sintered γ-GC/BT composite at varying weight ratios from 15% to 90% were identified by X-ray diffraction (XRD, RIGAKU smart lab) with Cu Kα (λ = 1.5418 Å) radiation in the range of 2θ = 10˚ to 80˚. The XRD results were compared to the JCPDS database. Moreover, LeBail refinement of the unit cell parameters was performed using JANA2006 software. The crystallite size estimation calculated for the corresponding phase was done by using the Scherrer Eq. (3)

$$L = \frac{K\lambda}{(FWHM \times cos\theta)} \quad (3)$$

where L refers to the crystallite size, K is the Scherrer constant (K = 0.94), λ is the wavelength of the radiation, θ is the diffraction angle of the peak, and $FWHM$ is the full width at half maximum.

The BT and γ-GC powders were subjected to Fourier-Transform Infrared Spectroscopy (FT-IR, SHI-MADZU, IRTracer-100) measurement in a transmission mode from 400 to 4000 cm^{-}

[1] with a resolution of 4 cm^{-1} to confirm the presence of functional groups. The morphology, particles size and grain size of untreated / heat-treated particles and cold-sintered γ-GC/BT composite were observed by field emission scanning electron microscopy (FE-SEM, TESCAN, model MIRA) and transmission electron microscopy (TEM, FEI, Model: TECNAI G2 20, Netherlands). In addition, energy dispersive X-ray spectroscopy (EDS-mapping) was performed to analyze the chemical components of materials. Particle size and particle size distribution were measured and analyzed through examination and quantitative analysis using ImageJ software. The three-dimensional (3D) X-ray image of the cold-sintered γ-GC/BT composite was obtained using Synchrotron Radiation X-ray Tomographic Microscopy (SR-XTM) technique at beamline 1.2 W, SLRI, Thailand. X-ray intensity was controlled by attenuating polychromatic X-rays with a 350 μm-thick aluminum foil. X-ray images were captured using a microscopic lens system and recorded by an sCMOS camera with a 1.44-μm pixel size. The X-ray images dataset was converted into sinograms, which were used in the Octopus Reconstruction software. The reconstructed images were visualized using Drishti software. The dielectric behavior, including dielectric constant (ε_r) and loss tangent (tan δ) of cold-sintered γ-GC/BT composites, was studied using an LCR meter (Agilent E4908A) from RT to 200 ˚ C at frequencies ranging from 100 Hz to 2MHz. The polarization versus electric field hysteresis (P-E) curves of cold-sintered γ-GC/BT composites were measured at RT by a standard ferroelectric test system (RT66A) from Radiant Technologies.

3 Results and Discussion

The morphology of the commercial nano-crystallites BT powder (untreated particles) is presented in Fig. 2(a), where SEM imaging showcases randomly distributed particles, with a smaller subset exhibiting homogeneously spherical-shaped particles of smaller size. ImageJ

analysis revealed a Gaussian distribution of particle sizes, indicating a relatively uniform particle size population. The mean particle size was determined to be 75.85 ± 13.65nm, with a narrow size distribution. The skewness and kurtosis values were close to zero, suggesting symmetry and a moderate peak, respectively. After the heat treatment process, agglomerates of varying sizes became apparent, as depicted in Fig. 2(d). The SEM images revealed a bimodal distribution with peak particle sizes observed at 1.39 ± 0.03 μm and 4.83 ± 0.11 μm. This distribution suggests the presence of two distinct populations of particles within the sample, possibly indicating different stages of aggregation or variations in particle formation mechanisms [24]. It's noteworthy that the heat-treated particles exhibit sizes within the micron range, which are more than 30 times larger compared to the untreated particles. BT particles of both nanometer and micrometer sizes will be mixed at a specific ratio determined by theoretical predictions for dense random packing. The TEM bright field image, the selected area electron diffraction (SAED) pattern, and the high-resolution TEM image (HRTEM) of BT powders before and after heat treatment at 1200 ˚ C for 12 h are shown in Fig 2(b)-(c), (e)-(f). For the untreated powder (Fig.2(b)), the particles appear nearly spherical with an average diameter of 78. 14 ± 19.12 nm. The inset SAED pattern shows a polycrystalline diffraction ring made up of separate diffraction spots, indicating the polycrystalline nature of the nanoparticles [25]. Further fringes in BT were detected by HR-TEM. Fig.2(c) exhibits lattice fringe with the interfering distance at 0.287 nm, which corresponds to the crystal plane (110) spacing of the cubic BT phase (JCPDS card no. 075-0213, $d_{(110)} = 0.283$ nm). In contrast, the BT powder, after heat treatment at 1200°C for 12 hours (Fig. 2e), demonstrates particle agglomeration, resulting in a tenfold increase in the average particle size compared to the untreated powder. The inset SAED pattern shows the bright spots assigned to the lattice atoms that were spaced crystallographically with perfect plan orientation of BT, suggesting high

crystallinity and structural perfection for the tetragonal perovskite structure [26]. Clear lattice fringes are observed (Fig.2(f)) with the measured interplanar spacing of about 0.286 nm corresponding to the crystallographic plane (101) of tetragonal BT (JCPDS card no. 079-2265, $d_{(101)}$ = 0.285) [27, 28]. These results confirmed that a high-temperature calcination results in the phase transformation of BT from cubic to tetragonal.

Moreover, the XRD pattern (Fig.2(g)) was consistent with the above results and the LeBail refinement. All the peaks (blue lines) are indexed (JCPDS card no. 079-2265) for cubic phase formation of the space group Pm-3m. The lattice parameters were a=b=c= 4.0067 Å and V = 65.3 Å. The parameters of refinement are R_p = 10.59, R_{wp} = 16.62 and GOF = 2.01. The R factors present a good agreement between refined and experimental XRD profiles for BT. The average crystallite sizes as estimated by Scherrer formula Eq. (3) was 20.33 nm using the (110) major diffraction peak. After calcination of BT at 1200 ˚C/12 h, the diffraction peaks (red line) are sharp and narrow, indicating high crystallinity. All peaks are indexed (JCPDS card no. 075-0213) for tetragonal phase, as judged from the splitting of the (200) diffraction plane into (002) and (200) at 51.02˚and 56.3˚, respectively. Lattice parameters were a = b = 3.9919 Å, c = 4.0321 Å and V = 64.3 Å, which belongs to space group of P4/mmm [29]. The parameters of refinement are R_p = 11.59, R_{wp} = 17.04 and GOF = 1.97. The average crystallite size was 27.56 ± 3.12 nm. These findings suggest that the tetragonal structure of BT phases is generated through high-temperature calcination.

The BT powder before and after calcination were characterized by FTIR in transmission mode as shown in Fig. 2(h). For the BT powder before calcination, the absorption bands appeared at 3507 cm^{-1}, which corresponded to the stretching mode of O-H groups. The band at 1637 cm^{-1} is characteristic of the O-H bending from the physically adsorbed water on BT nanoparticles. The

strong absorption at 487 cm^{-1} is assigned to the bending vibrations of the Ti-O bond in $[TiO_6]^{2-}$ octahedron. It is also a characteristic absorption of BT powder [30]. Notably, the intensity of the O-H stretching vibration bands at 3507 cm^{-1} and 1637 cm^{-1} became weaker as the calcination temperature increased, showing clearly instead the metal-oxygen (Ti-O) band stretching [31-33].

The γ-GC powder and the mixed BT powder were mixed at a varying weight ratio (15, 30, 50, and 90wt% of γ-GC powder) and grounded in a mortar, followed by addition of 7wt% of DI water and another grinding. Then, 0.3 g of the γ-GC/BT mixture was loaded into a tungsten carbide block, and a pressure of 10 MPa was applied. CSP was carried forward for 6 h before heating to 120 ˚C. At the end of the process, the tungsten carbide block was cooled, and the γ-GC/BT composite pellets were removed.

The white pellets, depicted in the inset of Fig. 3, possess a diameter of 1 cm and a thickness of approximately 0.7 mm. In the case of a composite sintered with 15wt% of γ-GC (Fig. 3(a)), the surface predominantly comprises 85wt% BT, resulting in densely packed BT particles and a smooth surface with reduced pore count. Subsequently, with an increase in γ-GC content to 30% (Fig. 3(b)), the surface remains smooth, albeit with small porous areas emerging. Upon further escalation of γ-GC content to 50wt% (Fig. 3(c)), the surface manifests large particle clusters, nanoparticle dispersion throughout the matrix, and some filling of gaps, leading to heightened porosity and surface unevenness. The average grain size measures 3.92 ± 1.75 μm. Notably, at 90wt% γ-GC (Fig. 3(d)), irregularly arranged large clumps of γ-GC particles, numerous small grain sizes (average grain size of 6.67 ± 4.17 μm), and substantial interparticle voids are observed. Additionally, nanoparticles are dispersed within the matrix. The SEM results underscore that an optimal γ-GC content of 15wt% fosters the formation of dense γ-GC/BT composites. Furthermore, SEM mapping and EDS analysis were conducted to explore the

chemical composition of the composites, leveraging X-ray emissions pertaining to the constituent elements. The presence of γ-GC and BT was confirmed by the detection of Ba, Ti, N, C, and O. SEM mapping of 15wt% γ-GC pellets (Fig. 4) reveals large agglomerations of Ba (Fig. 4(c)) and Ti (Fig. 4(d)), with gaps between them filled with Nitrogen (N) (Fig. 4(f)) and Carbon (C) (Fig. 4(g)), elements characteristic of γ-GC. Furthermore, EDS measurement (Fig. 4(h)) confirms the presence of Ba, Ti, O, N, and C elements in the composites, with Ba, Ti, and O comprising 41.2%, 18.4%, and 19.6% by weight, respectively. The Ba and Ti signals correspond to the BT content in 15wt% γ-GC pellets, affirming γ-GC's capacity to bind BT and form a ceramic composite via CSP.

The XTM images of the composites containing 5wt%, 30wt%, and 90wt% of γ-GC/BT were obtained using Synchrotron Radiation X-ray Tomographic Microscopy (SR-XTM). These images provide a macroscopic view of the 3D distribution of the components, distinguishing between two distinct phases represented by orange (γ-GC) and purple (BT). For the composites containing 5wt% γ-GC (Fig. 5(a)) and 30wt% γ-GC (Fig. 5(b)), BT acts as the matrix phase, with γ-GC evenly dispersed over the BT surface. Additionally, in certain regions, the γ-GC phase precipitates and fills the gaps between BT particles. However, as the γ-GC content increases to 90wt% (Fig. 5(c)), BT becomes uniformly distributed within the γ-GC matrix. The XTM image verifies that the γ-GC phase is dispersed throughout the specimen, with instances of agglomeration and precipitation between BT particles, a finding consistent with SEM observations. These XTM findings offer valuable insights into the spatial arrangement and distribution of γ-GC and BT phases within the composites, shedding light on their microstructural characteristics and providing essential information for understanding the composite's properties and behaviors.

The relative density of the γ-GC/BT composites, as determined by Eq. (1), is illustrated in Fig. 6(a). As the weight percentage of γ-GC increases from 15% to 90%, a corresponding trend of decreasing relative density is observed, declining from 96.7 ± 1.2% to 82.7 ± 1.1%. These findings align closely with the observations from SEM imaging. With a decrease in γ-GC content, the particles of BT exhibit a more compact arrangement compared to the composites containing 90wt% γ-GC, primarily due to the inherently higher density of BT. Furthermore, the presence of γ-GC serves to fill the interstitial spaces between BT particles, thereby reducing pore formation. This phenomenon contributes to the overall reduction in porosity and subsequent enhancement in relative density. The relative density can be explained by a mechanism as reported in the previous study [17]. It was found that pressure, sintering temperature, holding times, and transient liquid solvent are important factors for the effective CSP. BT powder is known to be thermodynamically unstable in water solutions. Ba^{2+} ions are leached out of the BT powder, producing a TiO_2-rich amorphous surface layer [34, 35]. The amorphous layer, which is difficult to dissolve in the liquid phase, impedes the dissolution-precipitation process during the CSP, thereby preventing the densification of the BT ceramic. Therefore, the surface of BT powders in this work was treated with acetic acid (CH_3COOH) to generate additional -OH groups on the BT particle surfaces (Fig. 6(b)) via hydroxylation reaction [36]. When the γ-GC powder is mixed with (acid-treated) BT particles and fabricated via CSP, hydrogen bond will form between the -COOH groups on the γ-GC chains and the -OH groups on the surfaces of BT particles [37, 38]. An appropriate amount of γ-GC can easily dissolve in water and act as the liquid phase, which enhances the dissolution-precipitation process during CSP. So, γ-GC promotes close packing in the composites and enhances the relative density of composites [39].

Furthermore, to elucidate the structural behavior, X-ray diffraction (XRD) analysis was employed to assess the cold-sintered samples, as depicted in Fig. 6(c). Notably, all sintered samples (15wt%, 30wt%, 50wt%, and 90wt% of γ-GC) manifest sharp diffraction peaks corresponding to two distinct phases: $BaTiO_3$ (tetragonal; JCPDS no. 075-0213) and γ-GC (JCPDS no. 06-230). At 90wt% of γ-GC, two prominent peaks observed at 25.28˚ and 31.57˚ can be unequivocally indexed to the (110) and (101) diffraction planes of γ-GC and BT respectively. As the γ-GC content decreases, notably, the intensity of the γ-GC peak at 25.28˚ undergoes a significant reduction, consistent with expectations. Subsequently, at γ-GC contents of 30wt% and 15wt%, the characteristic peaks associated with γ-GC are conspicuously absent from the diffraction patterns.

The cold-sintered samples underwent characterization using FTIR in transmission mode, with the results presented in Fig. 6(d). Across all sintered samples, distinct peaks indicative of γ-GC patterns emerged within the range of 1500-1200 cm^{-1}[40] . Notably, the highest intensity peak at 1573 cm^{-1} (peak 1) corresponds to the asymmetric (C=O)O stretching, while the peak at 1492 cm^{-1} (peak 2) signifies the NH bending vibration of NH_3^+. Additionally, the peak at 1390 cm^{-1} (peak 3) corresponds to the symmetric (C=O)O stretching, whereas the peak at 1328 cm^{-1} (peak 4) represents the CH_2 wagging with the lowest intensity. These observations collectively affirm the presence of γ-GC within the samples. However, a notable trend emerges as the γ-GC content decreases: the intensity of the four peaks diminishes significantly, accompanied by peak overlap within the range of 486-684 cm^{-1}. The overlapping peaks are attributed to the carboxylate ion group COO^- of γ-GC and the stretching vibrations of Ti-O of BT, further underscoring the formation of composites between γ-GC and BT. Importantly, no undesired phase transition of γ-GC was observed throughout the analysis, affirming the stability of the composite structure.

The density of composites, as elucidated in Fig. 7, is expounded through the schematic representation of the cold sintering mechanism across various stages. Initially, the composite material particles (I) comprising γ-GC, BT, and water are densely packed. In the initial stage, a sufficient quantity of the liquid phase (water) is integrated with the composite particles, ensuring homogeneous moisturization. Here, γ-GC particles act as a transient liquid phase, dissolving and diffusing alongside water, facilitating particle rearrangement (II). Notably, the pink frame in the illustration delineates the intricacies of particle sliding upon the introduction of the liquid phase, creating spaces at the particle-particle contact area. These spaces enable particle sliding and subsequent rearrangement. Densification primarily ensues under external pressure at this juncture, leading to overall sample shrinkage (S_1). Subsequently, in the second stage, a dissolution-precipitation process comes into play. Following particle dissolution, sliding, and rearrangement in the initial stage, mass transfer occurs via the diffusion of γ-GC ions or atoms along the water (III (a-ii)), effectively filling the interstitial gaps between grains. Consequently, precipitates (III(a-iii)) form on crystal sites with lower chemical potential, which are thermodynamically favored and conducive to neck growth. This mass transport process concurrently diminishes the surplus free energy of the surface and mitigates porosity, resulting in the formation of a dense solid and a slight sample shrinkage (S_2). The final stage, characterized by crystal growth (IV-b), is predominantly governed by a robust dynamic process catalyzed by water evaporation. This evaporation induces a supersaturated state of the liquid phase at temperatures slightly above its boiling point, thereby engendering a significant chemical driving force for the solid and liquid phases to attain equilibrium. Upon completion of precipitation, particle-particle contacts are markedly enhanced, facilitating crystal growth via the coalescence of small crystallites (Thickness = T_0) into larger ones (Thickness = T_1). The comprehensive overview of various BT-based ceramics and

composites, detailing their raw materials, the presence of transient liquid phases, CSP conditions, achieved densities, and corresponding references is present in Table I. BT ceramics synthesized through solid-state reactions typically undergo high-temperature sintering, yielding densities between 94-96%. Alternatively, employing $Ba(OH)_2 \cdot 8H_2O$ as a transient liquid phase at 180°C under pressure yields a density of 95%. Composite systems such as BT/ZnO and BT/Polytetrafluoroethylene exhibit densities ranging from 60%-98% and 93.5%, respectively, utilizing specific liquid phase chemistries and CSP conditions. Notably, the γ-GC/BT composites, synthesized at a lower temperature of 120°C and 10 MPa pressure, demonstrate a density of 96.7±1.6%. These findings highlight the diverse synthesis strategies and optimization approaches employed in the fabrication of BT-based ceramics and composites for various applications.

The dielectric responses of the γ-GC/BT composites were examined as a function of temperatures and frequency. Fig. 8(a) shows the temperature dependences of dielectric constant (ε_r) and dielectric loss (tan δ) for all composites from RT to 200 ˚C at 100 kHz. For the composites with 15-90 wt% γ-GC content, the value of ε_r tends to increase with increasing temperature. The maximum ε_r value obtained was 3600, and the low tan δ was 1.20 for 15wt% γ-GC composite. The increased ε_r value is a result of the addition of ferroelectric ceramic powders primarily caused by the dipolar polarization effect and induced by the permanent dipoles existent in the filler. The permanent dipole of BT is from the uneven distribution of the charge-density between O, Ba, and Ti atom [41].

The frequency-dependences of ε_r and tan δ of the composites are shown in Fig. 8(b) at 200 ˚C and the frequency from 100 Hz to 2 MHz. As frequency increases, ε_r decreases until it reaches a near-constant value at the high-frequency region. The high value of ε_r at low frequencies is caused by a combination of polarizations, including atomic, ionic, interfacial, and electronic.

However, only electronic polarization affects the ε_r at high frequencies. The results clearly show that when the amount of γ-GC decreases, the dipole of the interface increases due to the BT content increase and leading in an increase ε_r [42]. At 15wt% γ-GC, ε_r = 27,000 and tan δ (which is the lowest) was 1.50 at 100 Hz.

We also demonstrate the beneficial effect of increasing proportion of γ-GC by examining other presentations of AC properties, as depicted in Figure 8c, where the positive impact of γ-GC becomes more apparent. The imaginary part of the complex dielectric permittivity e'' (dash line in Figure 8c, shown for 90wt% as an example) follows the universal power law[43, 44] $e'' = A \cdot f^{s-1}$, where A and s are the fitting parameters. The parameter s represents the effective dimension of charge carriers,[45, 46] being 1D for s ~ 0.17-0.44. Accordingly, the s values of 0.11 (30wt% *g*-GC) and 0.22 (50wt% *g*-GC) suggest the 1D nature. Meanwhile, at 90% *g*-GC, the low s = 0.03 is close to zero such that e'' follows f^{-1}. This is the "low-frequency dispersion" [47, 48] which points out that very high charge densities are stored, consistent with the well-known capacitive nature of BT.

Figure 8d shows the T-dependent of the imaginary part of the complex electric modulus $M'' \times 100$ [$M'' = e''/(e'^2 + e''^2)$]. The electric modulus corresponds to the relaxation of an electric field in the material when the electric displacement remains constant.[47] It was found that the sample with 30wt%, 50wt%, and 90wt% g-GC had a relaxation peak at 87, 154, and 163 °C, respectively. The latter two might be compared to 132 °C obtained from the elastic (mechanical) modulus of BT sintered at 1300 °C.[48] The different peak temperatures might be explained by different sintering methods (CSP vs traditional) and measurement methods (electric relaxation vs mechanical relaxation). Still, the shift of the relaxation is clear, presumably to the value of BT. Table 2 presents a comparison of the dielectric properties of BT and BT composites that were

fabricated using CSP and traditional sintering methods. The results indicate that the dielectric properties of traditional sintered BT and γ-GC/BT composite are practically identical. Our study highlights the effectiveness of γ-GC as a transient liquid phase in CSP for the successful and sustainable production of high-density γ-GC/BT composites at relatively low temperatures.

The ferroelectric polarization-electric field (P-E) hysteresis loops of the γ-GC pellet and the γ-GC/BT composite pellets are shown in Fig. 8(e). It is found that the hysteresis loop of γ-GC/BT composite pellets becomes larger with increasing BT contents. Compared with γ-GC, the composite ceramics exhibit good symmetry and a well-saturated shape (see the inset). For 90wt% γ-GC, the surface has porosity, and the addition of BT makes the ferroelectric phase discontinuous as it hinders the domain orientation. However, as the γ-GC content decreases to 15wt%, the porosity is lower, and the ferroelectric property is optimized with easy switching of domains within materials. The measured values of the remnant polarization (P_r) and saturation polarization (P_s) at electric field of 20 $kV \cdot cm^{-1}$ are 0.013 $\mu C \cdot cm^{-2}$ and 0.025 $\mu C \cdot cm^{-2}$ for γ-GC, 0.035 $\mu C \cdot cm^{-2}$ and 0.052 $\mu C \cdot cm^{-2}$ for 90wt% γ-GC, 0.121 $\mu C \cdot cm^{-2}$ and 0.276 $\mu C \cdot cm^{-2}$ for 50wt% γ-GC, 0.554 $\mu C \cdot cm^{-2}$ and 1.466 $\mu C \cdot cm^{-2}$ for 15wt% γ-GC, respectively. In contrast, the coercive electric field (E_c) is lowest for pure γ-GC sample but increases for the 90wt% γ-GC. However, it was significantly decreased when the γ-GC content decreases further to 50wt% and 15wt% (Fig. 8(f)). Moreover, P_s clearly increases as the BT content increases. These results indicate that γ-GC as a transient liquid phase in a CSP can be successfully used to sustainably fabricate high-density composites between γ-GC and BT.

4 Conclusion

In this study, we have successfully demonstrated the implementation of organic ferroelectric (γ-GC) phase as a transient liquid phase substitute for fabricating the γ-GC/BT composite ceramic through CSP (Cold Sintering Process). Our investigation involved incorporating γ-GC contents ranging from 15% to 90% by weight into BT, followed by CSP with a sintering temperature of 120 ˚C, a holding time of 6 h, and an applied uniaxial pressure of 10 MPa. The addition of γ-GC resulted in notable enhancements in both relative density and electrical properties of the composites. Particularly, the optimal γ-GC content of 15wt% yielded a remarkable relative density of up to 96.7±1.6%. Our findings were further corroborated by FTIR and XRD analyses, which confirmed the phase stability of γ-GC and its prevention of undesired transformation into the non-piezoelectric phase (α-GC). SEM-EDS mapping revealed the precipitation-dissolution process of γ-GC in CSP, where it functioned as a filler diffusing into the space surrounding BT particles. XTM images provided a comprehensive 3D distribution of both BT and γ-GC, consistent with SEM observations. Furthermore, we conducted a thorough examination of the electrical properties of the composites across varying temperatures (RT-200 ˚C) and frequencies (100Hz-2MHz). The dielectric constant (ε_r) exhibited an increase with decreasing γ-GC content. Notably, the 15wt% γ-GC pellet demonstrated the highest ε_r of 3600 coupled with a low dielectric loss (tan δ) of 1.20. The P-E hysteresis loop measurements revealed that the 15wt% γ-GC composite ceramic displayed the highest values of P_s = 1.46 μC·cm^{-2} and P_r = 0.55 μC·cm^{-2}. Our study underscores the efficacy of γ-GC as a transient liquid phase in CSP for successfully and sustainably fabricating high-density γ-GC/BT composites at relatively low temperatures. These results contribute to the advancement of ceramic processing techniques and hold promise for various applications in the fields of electronics, energy, and beyond.

Acknowledgments

This study was financially supported by King Mongkut's Institute of Technology Ladkrabang (KMITL) under Grant Nos. KREF116501 and 2567-02-05-020. Jitrawan Noisak's work was funded by Grant No. KREF016412. Thitirat Charoonsuk's contributions were supported by the National Research Council of Thailand (NRCT) through Grant Number N42A650220. Pimchanok Ieamviteevanich's work received support from the School of Science at King Mongkut's Institute of Technology Ladkrabang. T. Bongkarn acknowledges financial assistance from Naresuan University, the National Science, Research, and Innovation Fund (NSRF) under Grant No. R2567B001, and the Global and Frontier Research University Fund at Naresuan University (NU) under Grant No. R2567C001. The collaboration between N. Vittayakorn and Te-Wei Chiu was facilitated by the NTU-KMITL-Joint Research Program under Grant No. KREF016412. We extend our appreciation to the Nanotechnology and Materials Analytical Instrument Service Unit (NMIS) at the College of Materials Innovation and Technology, KMITL, for their invaluable support and technical assistance.

Declaration of competing interest.

The authors have no competing interests to declare that are relevant to the content of this article.

References

1. Guo, H., et al., *Cold Sintering Process: A Novel Technique for Low-Temperature Ceramic Processing of Ferroelectrics.* Journal of the American Ceramic Society, 2016. **99**(11): p. 3489-3507.
2. Maria, J.-P., et al., *Cold sintering: Current status and prospects.* Journal of Materials Research, 2017. **32**(17): p. 3205-3218.

3. Yu, T., et al., *Current understanding and applications of the cold sintering process.* Frontiers of Chemical Science and Engineering, 2019. **13**: p. 654-664.
4. Wang, D., et al., *Cold sintering of microwave dielectric ceramics and devices.* Journal of Materials Research, 2021. **36**.
5. Anindy, U., M. Nur Indro, and I. Husein, *Piezoelectric properties: cerium oxide (CeO_2) doped barium titanate ($BaTiO_3$) film on ITO substrate.* Ferroelectrics, 2021. **570**(1): p. 162-175.
6. Kalugina, S.G., et al., *Fundamental optical spectra of ferroelectric $NaNO_2$.* Inorganic Materials, 2009. **45**(8): p. 925-929.
7. Guo, H., et al., *Protocol for ultralow-temperature ceramic sintering: an integration of nanotechnology and the cold sintering process.* ACS nano, 2016. **10**(11): p. 10606-10614.
8. Tsuji, K., et al., *Single Step Densification of High Permittivity $BaTiO_3$ Ceramics at 300 ºC.* Journal of the European Ceramic Society, 2019. **40**.
9. Kang, S., et al., *Barium titanate/poly (vinylidene fluoride) nanocomposites with core–shell structure with high dielectric constant and temperature stability prepared via a cold sintering process.* Journal of Materials Science: Materials in Electronics, 2020. **31**.
10. Ndayishimiye, A., et al., *Thermosetting polymers in cold sintering: The fabrication of ZnO‐polydimethylsiloxane composites.* Journal of the American Ceramic Society, 2020. **103**(5): p. 3039-3050.
11. Guo, J., et al., *Cold sintered ceramic nanocomposites of 2D MXene and zinc oxide.* Advanced Materials, 2018. **30**(32): p. 1801846.
12. Alter, H., *Filler particle size and mechanical properties of polymers.* Journal of Applied Polymer Science, 1965. **9**(4): p. 1525-1531.
13. Zhao, Y., et al., *Cold-Sintered V_2O_5-PEDOT:PSS Nanocomposites for Negative Temperature Coefficient Materials.* Journal of the European Ceramic Society, 2018. **39**.
14. Sada, T., et al., *High permittivity $BaTiO_3$ and $BaTiO_3$-polymer nanocomposites enabled by cold sintering with a new transient chemistry: $Ba(OH)_2 \cdot 8H_2O$.* Journal of the European Ceramic Society, 2021. **41**(1): p. 409-417.
15. Vinoth, S. and S.-F. Wang, *Cold Sintering Process for a $BaTiO_3$/Poly (vinylidene difluoride) Ceramic–Polymer Composite: Evaluation of the Structural and Microwave Dielectric Properties.* Inorganic Chemistry, 2023.

16. Sada, T., et al., *Highly Reliable $BaTiO_3$ - Polyphenylene Oxide Nanocomposite Dielectrics via Cold Sintering.* Advanced Materials Interfaces, 2021. **8**(18): p. 2100963.
17. Noisak, J., et al., *Towards the preparation of organic ferroelectric composites: fabrication of a gamma-glycine-bacterial cellulose composite via cold sintering process.* Journal of Materials Research and Technology, 2023. **25**: p. 4749-4760.
18. Peter, M.E. and P. Ramasamy, *Growth of gamma glycine crystal and its characterisation.* Spectrochimica Acta Part A: Molecular and Biomolecular Spectroscopy, 2010. **75**(5): p. 1417-1421.
19. Ukasi, S., et al., *Gamma glycine enhances efficiency of organic hybrid piezoelectric-triboelectric nanogenerators.* Nano Energy, 2024. **119**: p. 109045.
20. Bouchard, A., G.W. Hofland, and G.-J. Witkamp, *Solubility of Glycine Polymorphs and Recrystallization of β-Glycine.* Journal of Chemical & Engineering Data, 2007. **52**(5): p. 1626-1629.
21. Yang, X., X. Wang, and C. Ching, *Solubility of Form α and Form γ of Glycine in Aqueous Solutions.* Journal of Chemical and Engineering Data - J CHEM ENG DATA, 2008. **53**.
22. Guo, N., H.-Z. Shen, and P. Shen, *Cold sintering of chitosan/hydroxyapatite composites.* Materialia, 2022. **21**: p. 101294.
23. Evans, H., *An X-ray diffraction study of tetragonal barium titanate.* Acta Crystallographica, 1961. **14**(10): p. 1019-1026.
24. Su, J. and J. Zhang, *Recent development on modification of synthesized barium titanate ($BaTiO_3$) and polymer/$BaTiO_3$ dielectric composites.* Journal of Materials Science: Materials in Electronics, 2019. **30**(3): p. 1957-1975.
25. Fuentes, S., et al., *Synthesis and characterization of $BaTiO_3$ nanoparticles in oxygen atmosphere.* Journal of Alloys and Compounds, 2010. **505**(2): p. 568-572.
26. Vasudevan, R., et al., *Effect of microwave sintering on the structural, optical and electrical properties of $BaTiO_3$ nanoparticles.* Journal of Materials Science: Materials in Electronics, 2014. **25**.
27. Hu, Z., et al., *Facile fabrication of tetragonal phase single-crystalline $BaTiO_3$ terrace-like dendrite by a simple solvothermal method and its piezocatalytic properties.* Materials Chemistry and Physics, 2023. **293**: p. 126911.

28. Luo, G., et al., *Synthesis of tetragonal $BaTiO_3$ powder with size and dispersity optimization via synergy mechanisms of combined dispersants.* Journal of Alloys and Compounds, 2023. **944**: p. 169079.
29. Luan, S., et al., *Fabrication of $BaTiO_3$ nanopowders with high tetragonality via two-step assisted rotary furnace calcination for MLCC applications.* Ceramics International, 2023. **49**(8): p. 12529-12539.
30. Thi Tuyet Mai, P., et al., *Enhancement of Polarization Property of Silane-Modified $BaTiO_3$ Nanoparticles and Its Effect in Increasing Dielectric Property of Epoxy/$BaTiO_3$ Nanocomposites.* Journal of Science: Advanced Materials and Devices, 2016. **1**: p. 90-97.
31. Lee, D., et al., *Effect of calcination temperature and atmosphere on crystal structure of $BaTiO_3$ nanofibers.* Metals and Materials International - MET MATER INT, 2010. **16**: p. 453-457.
32. Hao, S., et al., *Preparation and Characterization of Ag-Doped $BaTiO_3$ Conductive Powders.* International Journal of Inorganic Chemistry, 2011. **2011**.
33. Nakhaei, M. and A. Bahari, *Synthesis and investigation of temperature effects on barium titanate ($BaTiO_3$) nanostructural and electrical properties.* Journal of Materials Science: Materials in Electronics, 2016. **27**.
34. Chiang, C.-W. and J.-H. Jean, *Effects of barium dissolution on dispersing aqueous barium titanate suspensions.* Materials Chemistry and Physics, 2003. **80**(3): p. 647-655.
35. Tripathy, S.S. and A.M. Raichur, *Dissolution properties of $BaTiO_3$ nanoparticles in aqueous suspensions.* Journal of Experimental Nanoscience, 2011. **6**(2): p. 127-137.
36. Chang, S.-J., et al., *An efficient approach to derive hydroxyl groups on the surface of barium titanate nanoparticles to improve its chemical modification ability.* Journal of Colloid and Interface Science, 2009. **329**(2): p. 300-305.
37. Nawanil, C., et al. *Effect of surface treatment on electrical properties of barium titanate/carbon nanotube/polydimethylsiloxane nanocomposites*. in *AIP Conference Proceedings*. 2018. AIP Publishing.
38. Chen, L., et al., *Mechanical, thermal, and dielectric properties of polyvinylidene fluoride nanocomposites fabricated by introducing functional MWCNTs/barium titanate compounding dielectric nanofillers.* Polymer Composites, 2021. **42**(3): p. 1383-1395.

39. Kang, S., et al., *Influence of surface coating on the microstructures and dielectric properties of $BaTiO_3$ ceramic via a cold sintering process.* RSC Advances, 2020. **10**(51): p. 30870-30879.
40. R, E.V., et al., *Crystal growth, optical and thermal studies of nonlinear optical-glycine single crystal grown from lithium nitrate.* Optik - International Journal for Light and Electron Optics, 2012. **123**: p. 409-413.
41. Stefanescu, E.A., et al., *Multifunctional fiberglass-reinforced PMMA-$BaTiO_3$ structural/dielectric composites.* Polymer, 2011. **52**(9): p. 2016-2024.
42. Chao, F., et al., *Study of dielectric property on $BaTiO_3$/BADCy composite.* Materials Chemistry and Physics, 2008. **108**: p. 306-311.
43. Maluangnont, T., et al., *Electrochemical and electrical characteristics of ball milled $Cs_2Ti_6O_{13}$ modified by the surface-to-bulk migration of hydroxyl groups.* Dalton Trans., 2023. **52**: p. 11815-11825.
44. Sriphan, S., et al., *Effect of adsorbed water and temperature on the universal power law behavior of lepidocrocite-type alkali titanate ceramics.* J. Phys. Chem. C, 2021. **125**: p. 12910–12920.
45. Dyre, J.C., et al., *Fundamental questions relating to ion conduction in disordered solids.* Rep. Prog. Phys., 2009. **72**: p. 046501.
46. Sidebottom, D.L., *Dimensionality dependence of the conductivity dispersion in ionic materials.* Phys. Rev. Lett., 1999. **83**: p. 983-986.
47. Liu, J., et al., *Dielectric permittivity and electric modulus in $Bi_2Ti_4O_{11}$* J. Chem. Phys., 2003. **119**: p. 2812-2819.
48. Cheng, B.L., et al., *Mechanical loss and elastic modulus associated with phase transitions of barium titanate ceramics.* J. Alloys Compd., 1994. **211/212**: p. 352-355.
49. Shao, S., et al., *High piezoelectric properties and domain configuration in $BaTiO_3$ ceramics obtained through the solid-state reaction route.* Journal of Physics D: Applied Physics, 2008. **41**(12): p. 125408.
50. Kim, H.T. and Y.H. Han, *Sintering of nanocrystalline $BaTiO_3$.* Ceramics International, 2004. **30**(7): p. 1719-1723.
51. Chaisan, W., *Effect of sintering temperature on the hysteresis properties of barium titanate ceramic.* NU. International Journal of Science, 2007. **4**(2): p. 132-139.

52. Guo, H., et al., *Hydrothermal-Assisted Cold Sintering Process: A New Guidance for Low-Temperature Ceramic Sintering.* ACS Appl Mater Interfaces, 2016. **8**(32): p. 20909-15.
53. Coutinho, L., R. Aredes, and E. Antonelli, *Cold sintering and electric characterization of ZnO-$BaTiO_3$ composites.* Cerâmica, 2021. **67**: p. 105-110.
54. Sada, T., et al., *High permittivity $BaTiO_3$ and $BaTiO_3$-polymer nanocomposites enabled by cold sintering with a new transient chemistry: $Ba(OH)_2 \cdot 8H_2O$.* Journal of the European Ceramic Society, 2021. **41**(1): p. 409-417.
55. Sada, T., et al., *Highly Reliable $BaTiO_3$-Polyphenylene Oxide Nanocomposite Dielectrics via Cold Sintering.* Advanced Materials Interfaces, 2021. **8**(18): p. 2100963.
56. Vinoth, S. and S.-F. Wang, *Cold Sintering Process for a $BaTiO_3$/Poly (vinylidene difluoride) Ceramic–Polymer Composite: Evaluation of the Structural and Microwave Dielectric Properties.* Inorganic Chemistry, 2023. **62**(21): p. 8326-8333.
57. Sada, T., et al., *Surface modification of $BaTiO_3$ with catechol surfactant and effects on cold sintering.* Journal of Applied Physics, 2021. **129**(18).

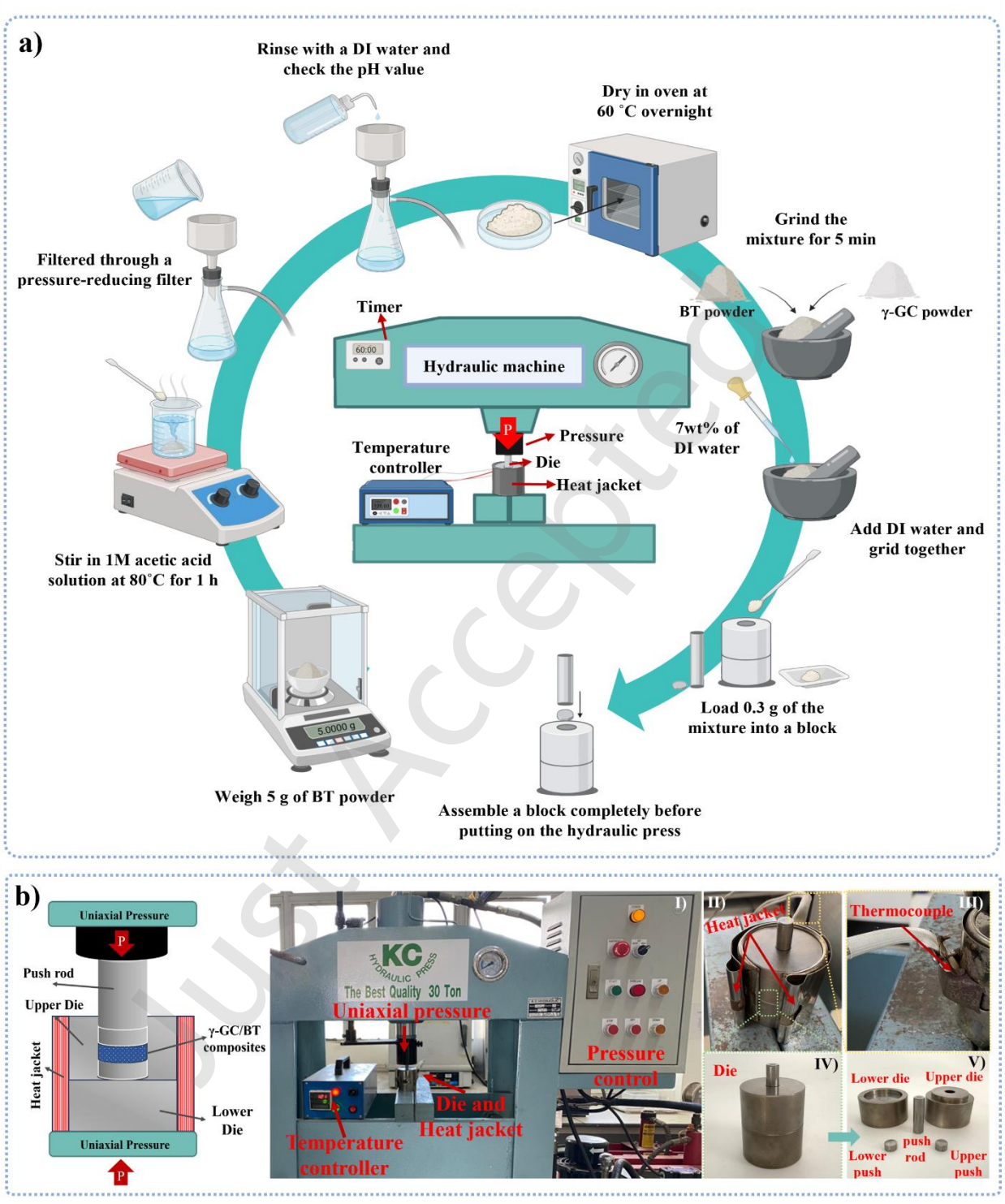

Fig. 1 Schematic illustration of the fabrication process of the γ-GC/BT composite via CSP.

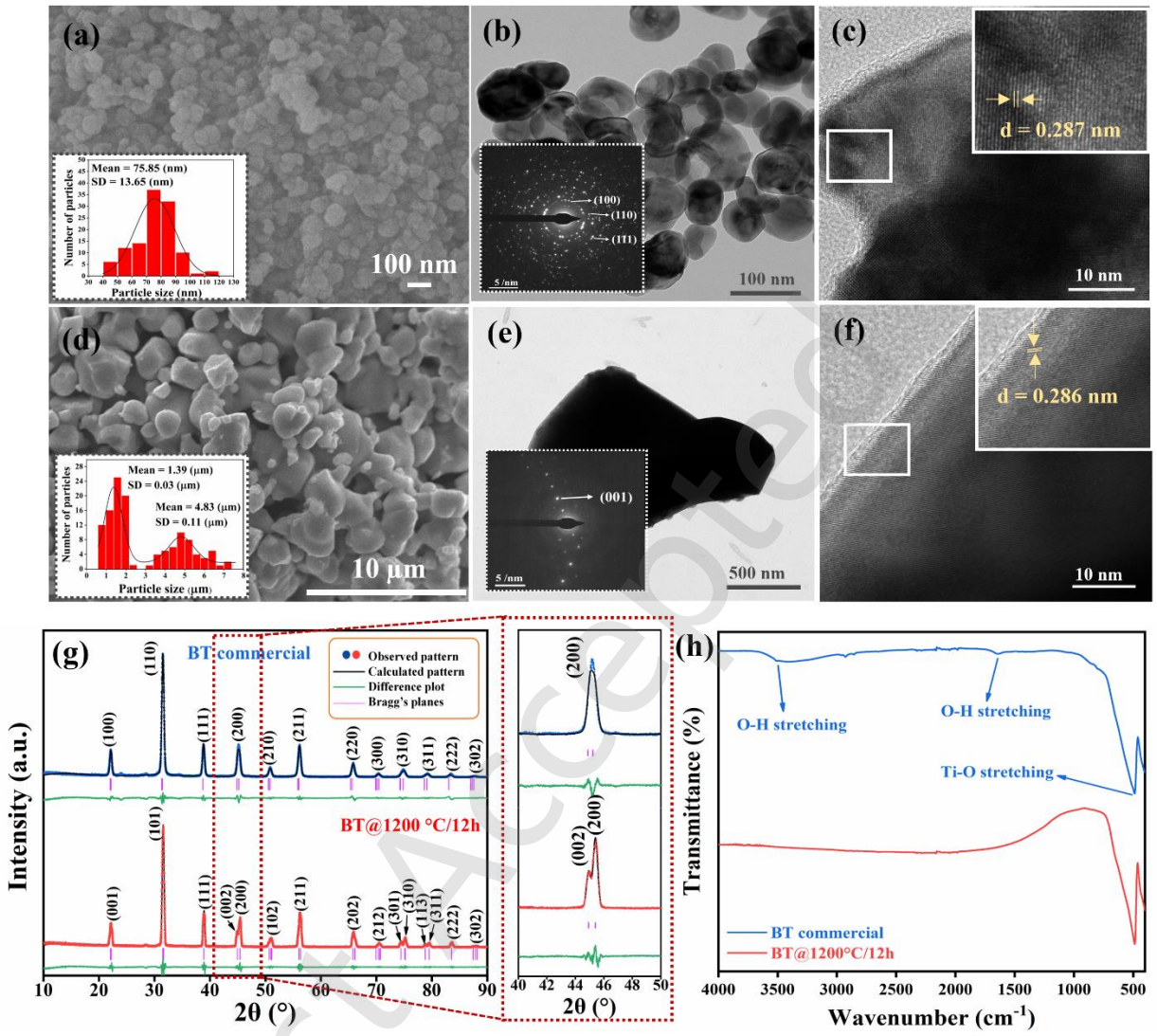

Fig. 2 SEM images of (a) BT commercial powder before calcination and (d) BT after calcination at 1200 ˚C for 12 h. (b), (e) show TEM images of BT powder before and after calcination at 1200 ˚C for 12 h respectively. The inset shows the corresponding SAED patterns. (c), (f) the high-resolution TEM and the white frame showing the lattice fringe. (g), (h) XRD and FTIR results of BT powder before and after calcination at 1200 ˚C for 12 h.

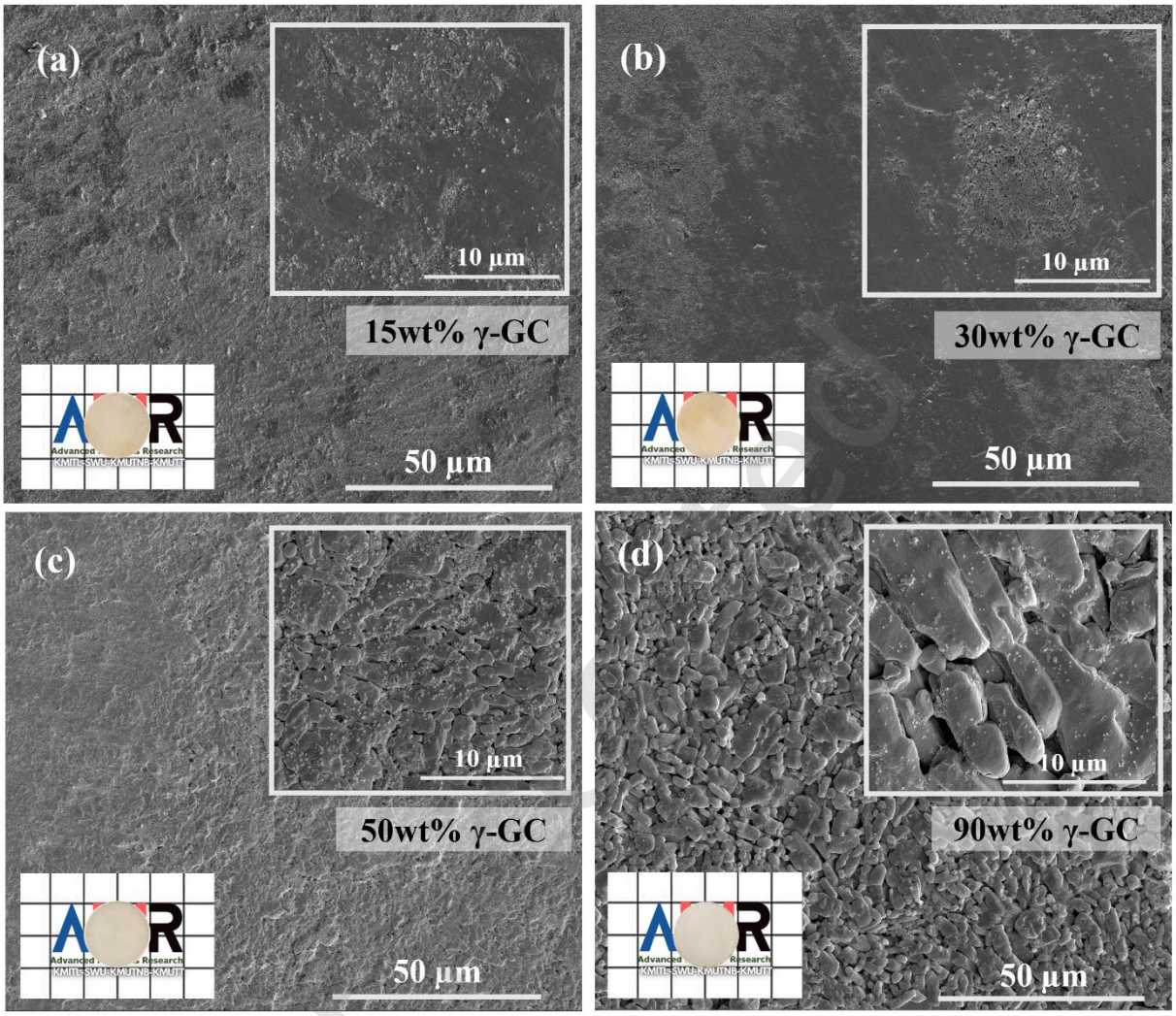

Fig. 3 SEM images of cold-sintered composites between γ-GC and BT as prepared through CSP at varying amount of γ-GC: (a) 15wt% (b) 30wt% (c) 50wt% and (d) 90wt%. The bottom-left insets show the corresponding digital image of the pellet. The white frame on top-right shows morphological features under 10,000 x magnification.

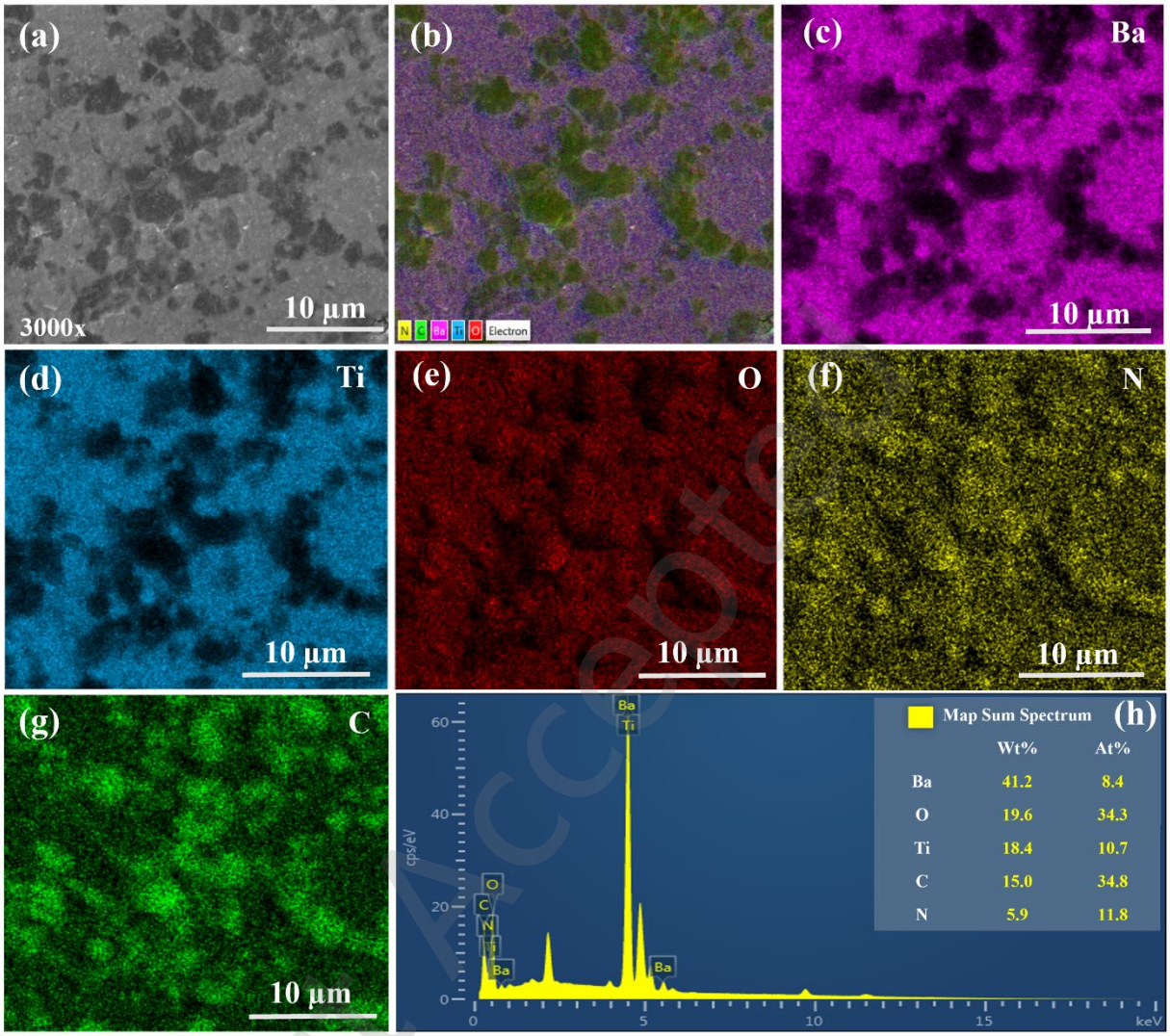

Fig. 4 The SEM-EDS mapping of 15wt% γ-GC pellet: (a) SEM image at a magnification of 3000x for the composite 15wt% γ-GC/BT. (b) All mapping elements. (c-g) Mapping image of Ba, Ti, O, N, and C element in the composites. (h) The EDS spectrum with the table in the inset showing a quantitative result obtained for Ba, O, Ti, C, and N.

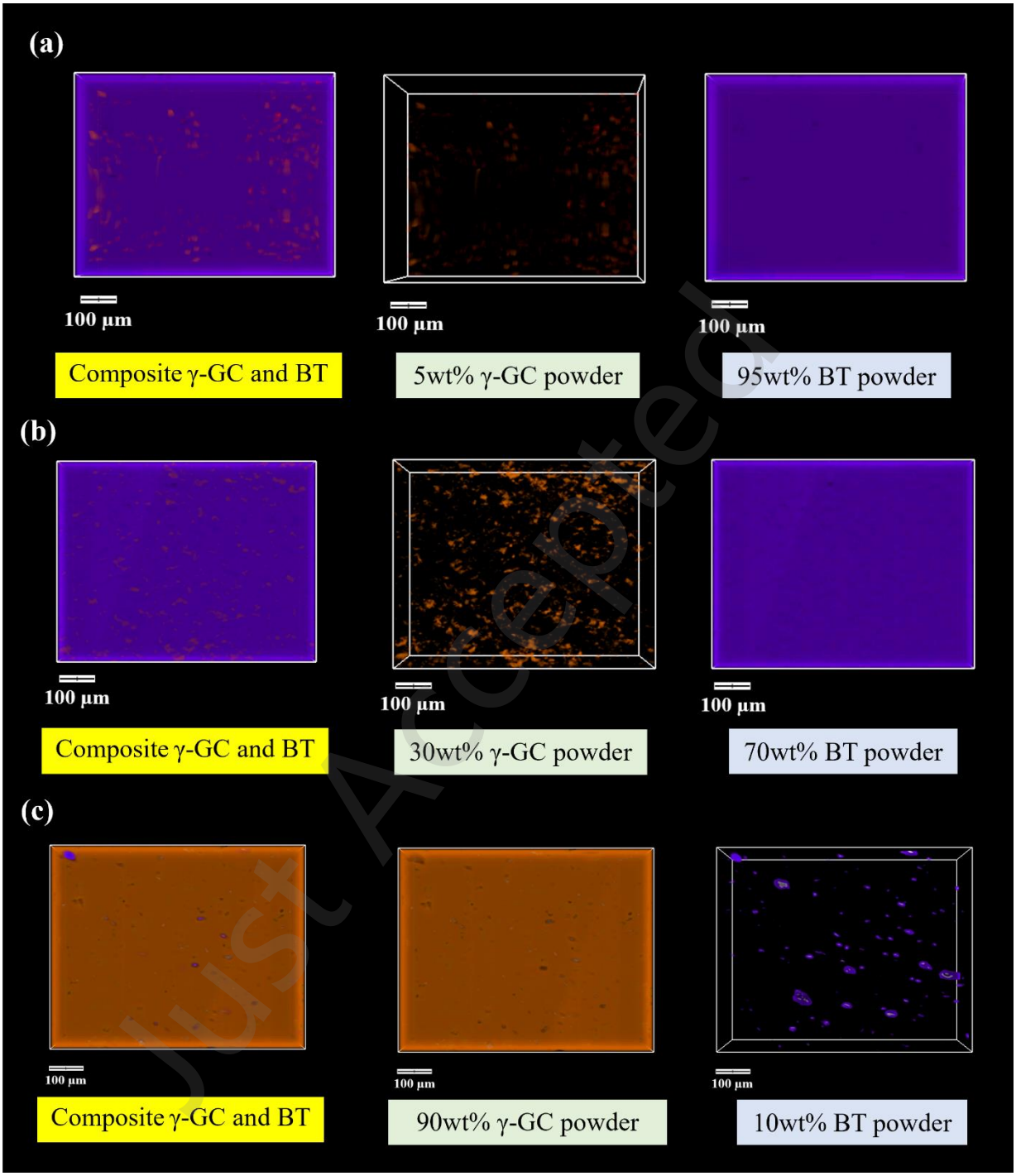

Fig. 5 X-ray tomographic 3D visualization of γ-GC/BT composites via CSP at varying γ-GC contents (a) 5wt% (b) 30wt% and (c) 90wt% respectively.

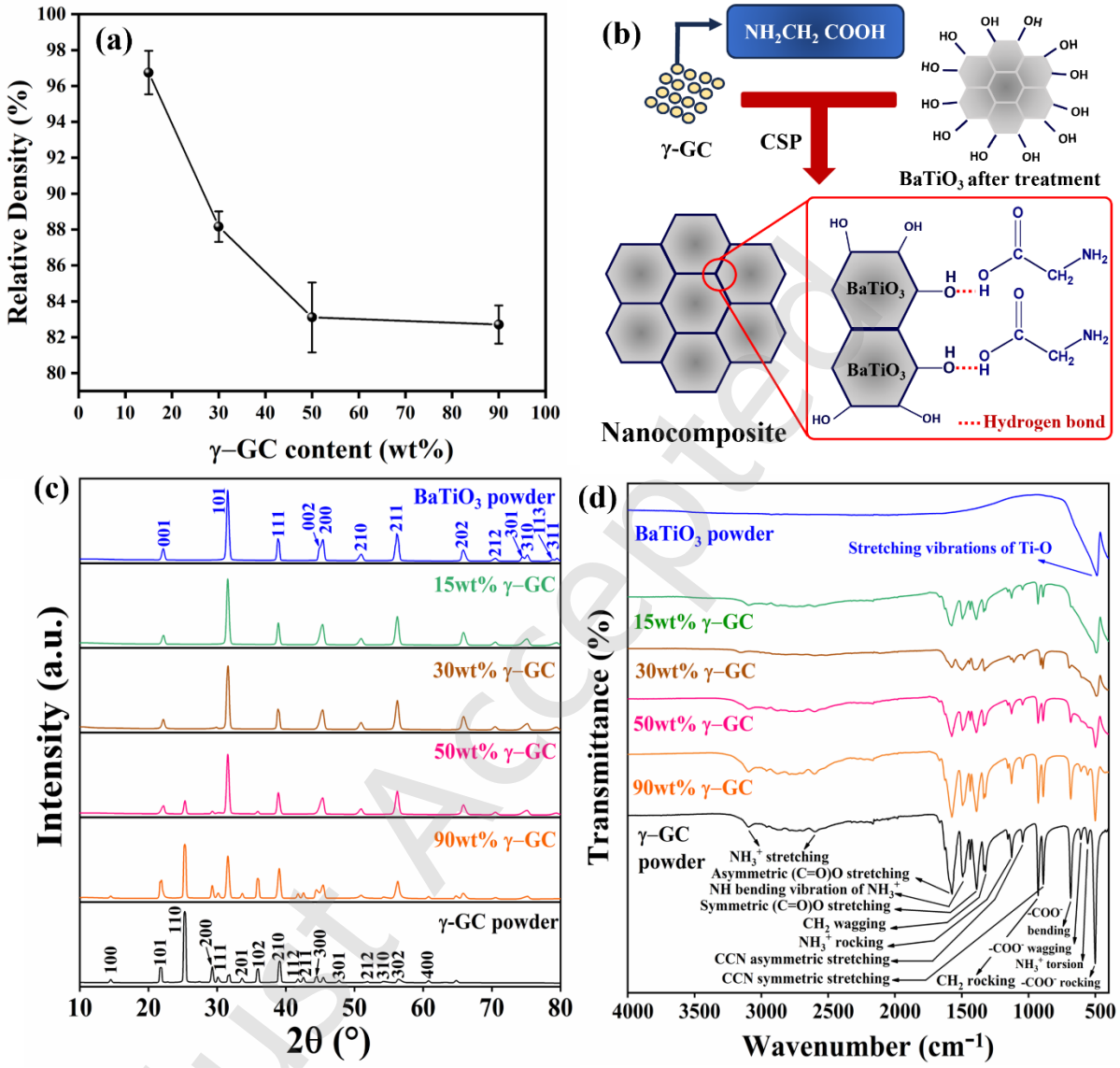

Fig. 6 The relative density of γ-GC/BT composites after CSP (a) variation of the γ-GC contents. (b) schematic diagram of BT after treatment with 1 M acetic acid, showing the surface OH group on BT surfaces and the formation of hydrogen bond in the γ-GC/BT composite, (c) XRD patterns and (d) FTIR spectrum of γ-GC/BT composites.

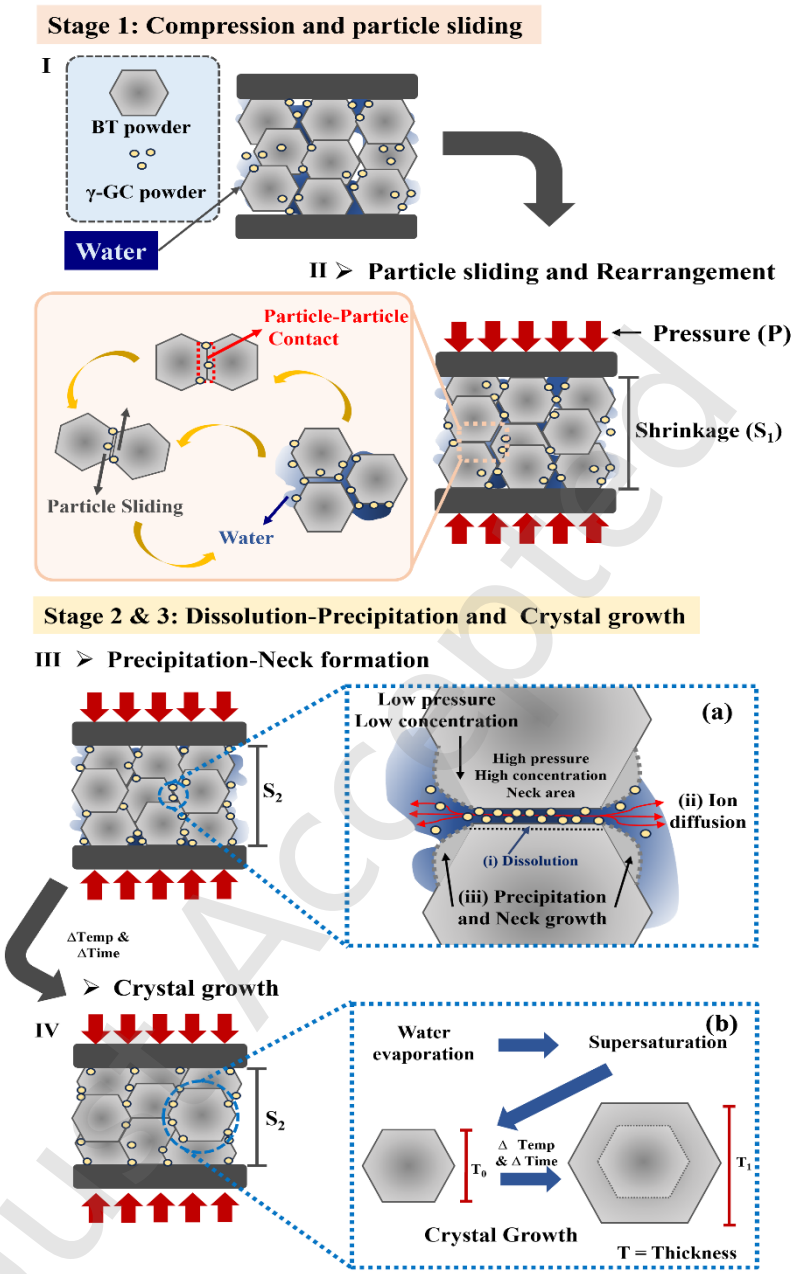

Fig. 7 Schematics of CSP mechanism at mainly 3 stages adapted from Refs.[1, 4, 17]. Stage 1 involves I. particle compaction of composite consisting of γ-GC, BT, and water, II. Particle sliding and rearrangement. Stage 2 shows the dissolution-precipitation process, III. Precipitation-Neck formation. Details of this stage show in (a) dissolution (i), ion diffusion (ii), precipitation-neck growth (iii). Stage 3 related to crystal growth (IV) and (b) show the detail of its stage related to water evaporation and crystal growth.

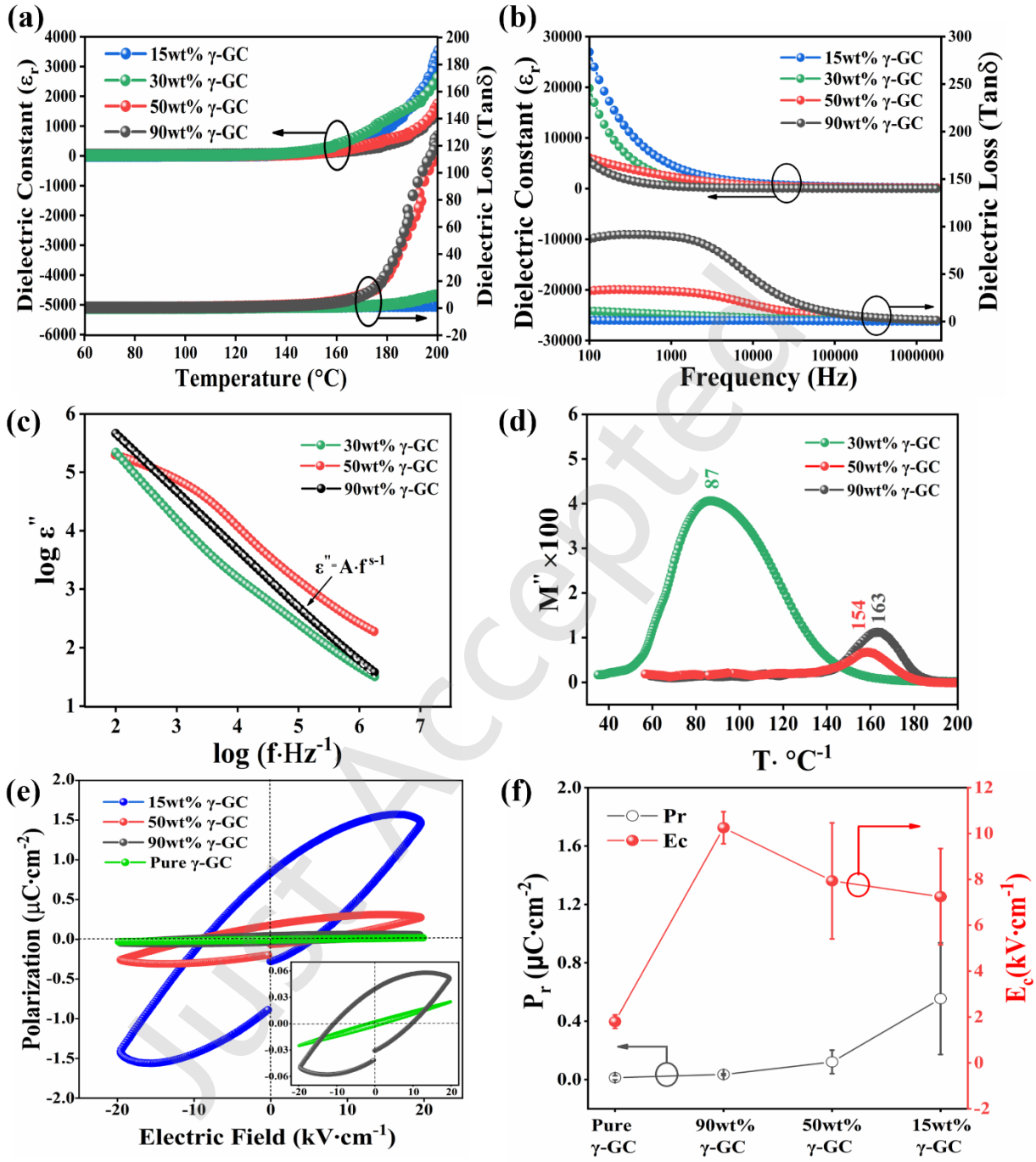

Fig. 8 Electrical properties of γ-GC/BT composites fabricated via CSP: (a) temperature-dependence (b) frequency-dependence of the dielectric constant and dielectric loss. (c) P-E hysteresis loop of γ-GC and the γ-GC/BT composites, at the electric field of 20 kV/cm, and (d) the corresponding P_r and E_c values.

Table 1. A concise comparison of the raw materials used, the presence of transient liquid phase, and the conditions of the Cold Sintering Process (CSP) for both BT-based ceramics and composites.

BT-based Ceramics/Composite	Raw materials	Transient liquid phase	CSP conditions	density	Reference
$BaTiO_3$ (Solid state reaction)	$BaCO_3$+TiO_2	-	1200-1400 ˚ C/ 6-24 h (Traditional sintering temperature)	94-96%	[49, 50] [51]
$BaTiO_3$	$Ba(OH)_2$+TiO_2 → $BaTiO_3$	$Ba(OH)_2 \cdot 8H_2O$	180 ˚ C/ 15 to 120 mins/430 MPa/annealing 900 ˚ C	95%	[52]
$BaTiO_3$/ZnO	$BaTiO_3$ + ZnO	CH_3COOH + H_2O	250˚C/1h/166 MPa	60%-98%	[53]
$BaTiO_3$/Polytetrafluoroethylene (PTFE) composites	Nano $BaTiO_3$/polymer PTFE	$Ba(OH)_2 \cdot 8H_2O$	225˚C/2h/350 MPa	93.5%	[54]
$BaTiO_3$/Polyphenylene oxide nanocomposite	$BaTiO_3$/polymer PPO	$Ba(OH)_2 \cdot 8H_2O$	225˚C/12h/350 MPa	96%	[55]
$BaTiO_3$/Poly(vinylidene difluoride)	$BaTiO_3$/polymer PVDF	H_2O	190˚C/160 mins/350 MPa	94.8%	[56]
$BaTiO_3$/ catechol	Nano$BaTiO_3$/benzenediol organic compound	$Ba(OH)_2 \cdot 8H_2O$	200˚C/75 mins/350 MPa/annealing 200 ˚ C	93%-95%	[57]
γ-GC/BT composites	Micro/Nano $BaTiO_3$	γ-$C_2H_5NO_2$	120 ˚C /6 hrs/10 MPa	96.7±1.6%	This study

Table 2. Comparison of Dielectric Properties of BT ceramic and BT-Based Composites prepared by CSP.

System	Fabrication process	Dielectric constant at 1kHz	Dielectric loss at 1kHz	Reference
$BaTiO_3$	Solid state reaction	2900-4500	1.4-2.8	[49, 50] [51]
$BaTiO_3$	CSP	1,800	0.03	[52]
$BaTiO_3$/ZnO	CSP	50.9-7000	0.04-3.13	[53]
$BaTiO_3$/Polytetrafluoroethylene (PTFE) composites	CSP	790 (@ 1 MHz)	1.4 (@ 1 MHz)	[54]
$BaTiO_3$/Polyphenylene oxide nanocomposite	CSP	1,500	0.05	[55]
$BaTiO_3$/Poly(vinylidene difluoride)	CSP	71.1 (@ 1 GHz)	0.04 (@ 1 GHz)	[56]
$BaTiO_3$/ catechol	CSP	700 (@ 1 MHz)	0.04 (@ 1 MHz)	[57]
γ-GC/BT composites	CSP	4500	0.99	This study